Simulating Solar Maximum Conditions Using the Alfven Wave Solar-Atmosphere Model (AWSoM)

Nishtha Sachdeva[1,1], Gábor Tóth[1,1], Ward B Manchester[1,1], Bart Van Der Holst[1,1], Zhenguang Huang[1,1], Igor V Sokolov[1,1], Lulu Zhao[1,1], Qusai Al-Shidi[1,1], Yuxi Chen[1,1], Tamas I Gombosi[1,1], and Carl J Henney[2,2]

[1]University of Michigan
[2]Kirtland AFB

November 30, 2022

Abstract

To simulate solar Coronal Mass Ejections (CMEs), predict their time of arrival and geomagnetic impact, it is important to accurately model the background solar wind conditions in which CMEs propagate. We use the Alfvén Wave Solar-atmosphere Model (AWSoM) within the the Space Weather Modeling Framework (SWMF) to simulate solar maximum conditions during two Carrington rotations and produce solar wind background conditions comparable to the observations. We describe the inner boundary conditions for AWSoM using the ADAPT global magnetic maps and validate the simulated results with EUV observations in the low corona and measured plasma parameters at L1 as well as at the position of the STEREO spacecraft. This work complements our prior AWSoM validation study for solar minimum conditions Sachdeva et al. (2019), and shows that during periods of higher magnetic activity, AWSoM can reproduce the solar plasma conditions (using properly adjusted photospheric Poynting flux) suitable for providing proper initial conditions for launching CMEs.

1

Simulating Solar Maximum Conditions Using the Alfvén Wave Solar-Atmosphere Model (AWSoM)

Nishtha Sachdeva,[1] Gábor Tóth,[1] Ward B. Manchester,[1] Bart van der Holst,[1] Zhenguang Huang,[1]
Igor V. Sokolov,[1] Lulu Zhao,[1] Qusai Al Shidi,[1] Yuxi Chen,[1] Tamas I. Gombosi,[1] Carl J. Henney,[2]
Diego G. Lloveras,[3] and Alberto M. Vásquez[3, 4]

[1]Department of Climate and Space Sciences and Engineering, University of Michigan, Ann Arbor, MI 48109, USA
[2]AFRL/Space Vehicles Directorate, Kirtland AFB, NM, USA
[3]Instituto de Astronomía y Física del Espacio, CONICET-University of Buenos Aires, Ciudad de Buenos Aires, CC 67-Suc 28, Argentina
[4]Departamento de Ciencia y Tecnología, Universidad Nacional de Tres de Febrero, Buenos Aires, Argentina

Submitted to ApJ

ABSTRACT

To simulate solar Coronal Mass Ejections (CMEs), predict their time of arrival and geomagnetic impact, it is important to accurately model the background solar wind conditions in which CMEs propagate. We use the Alfvén Wave Solar-atmosphere Model (AWSoM) within the the Space Weather Modeling Framework (SWMF) to simulate solar maximum conditions during two Carrington rotations and produce solar wind background conditions comparable to the observations. We describe the inner boundary conditions for AWSoM using the ADAPT global magnetic maps and validate the simulated results with EUV observations in the low corona and measured plasma parameters at L1 as well as at the position of the STEREO spacecraft. This work complements our prior AWSoM validation study for solar minimum conditions Sachdeva et al. (2019), and shows that during periods of higher magnetic activity, AWSoM can reproduce the solar plasma conditions (using properly adjusted photospheric Poynting flux) suitable for providing proper initial conditions for launching CMEs.

Keywords: interplanetary medium — magnetohydrodynamics (MHD) — methods: numerical — solar wind — Sun: corona — waves

1. INTRODUCTION

Large scale eruptions of solar coronal plasma and magnetic fields expelled into the solar wind, so called coronal mass ejections (CMEs), are major drivers of space weather. When directed towards the Earth, CMEs can lead to severe geomagnetic effects that can threaten advanced technology that we are highly reliant on. It is therefore important to improve their time of arrival and impact predictions at the Earth. The first step towards modeling CMEs is to determine the plasma environment these CMEs propagate through.

Many magnetohydrodynamic(MHD)-based models of the solar corona have had success in modeling the solar wind background and propagating CMEs. Various analytical and numerical models developed in the past few decades simulate the solar coronal background (Mikić et al. 1999; Groth et al. 2000; Roussev et al. 2003; Cohen et al. 2007; Feng et al. 2011; Evans et al. 2012), which facilitates the CME propagation to provide predictions. Several coronal models are based on Alfvén wave turbulence, which was discovered some 50 years ago (Coleman 1968; Belcher & Davis 1971). The first physics-based 1D models of the solar corona that include turbulence are Belcher & Davis (1971); Alazraki & Couturier (1971). These were followed by two-dimensional models (Bravo & Stewart 1997; Ruderman et al. 1998; Usmanov et al. 2000) and more recently, three-dimensional (3D) models have been developed (Lionello et al. 2009; Downs et al. 2010; van der Holst et al. 2010) that include Alfvén wave turbulence. The physics processes included in these models have also advanced, with non-linear interactions between forward propagating and reflected Alfvén waves to describe coronal heating studied by Velli et al. (1989); Zank, Matthaeus & Smith (1996); Matthaeus et al. (1999); Suzuki & Inutsuka (2006); Ver-

Corresponding author: Nishtha Sachdeva
nishthas@umich.edu

dini & Velli (2007); Cranmer (2010); Chandran et al. (2011); Matsumoto & Suzuki (2012). Extended MHD (XMHD) models also include heat conduction, radiative losses and energy partitioning among particle species as well as temperature anisotropy (Leer & Axford 1992; Chandran et al. 2011; Vásquez et al. 2003; Li et al. 2004; Sokolov et al. 2013; van der Holst et al. 2014). XMHD models are therefore capable of predicting both electron and proton (parallel and perpendicular) temperatures, turbulent wave amplitudes in the solar wind as well as the wave reflection and dissipation rates. These advances in 3D MHD modeling have provided the capability to study the evolution of the solar wind and solar transients as they propagate from the solar corona into the heliosphere (Kilpua, Koskinen & Pulkkinen 2017; Manchester et al. 2017; Gombosi et al. 2018, 2021).

Similarly, models have benefited by the increased availability of extensive observational resources such as the Solar Dynamics Observatory/Atmospheric Imaging Assembly (SDO/AIA; Lemen et al. 2012), SDO/Helioseismic Magnetic Imager (SDO/HMI; Schou et al. (2012)), Solar-Terrestrial Relations Observatory (STEREO, Howard et al. 2008), Solar and Heliospheric Observatory/Large Angle and Spectrometric COronagraph (SOHO/LASCO; Brueckner et al. 1995), Advance Composition Explorer (ACE), WIND and Geotail are used to drive and validate these models.

Sachdeva et al. (2019) describes the Alfvén Wave Solar atmosphere Model (AWSoM), a component within the Space Weather Modeling Framework (SWMF; Tóth et al. 2012; Gombosi et al. 2021), simulations and their validation for solar wind conditions during a period of low solar activity. AWSoM is a 3D extended data-driven MHD model incorporating observational maps of the photospheric magnetic field. Our AWSoM simulated results for solar minimum using Air Force Data Assimilation Photospheric Flux Transport - Global Oscillation Network Group (ADAPT-GONG) maps were validated against a comprehensive suite of observations between the low corona and 1 AU. AWSoM model results have also been compared to *in situ* observations from ACE, Wind and STEREO data at 1 AU (Meng et al. 2015; van der Holst et al. 2019) and to observations from *Ulysses* (Oran et al. 2013; Jian et al. 2016).

In this paper, we continue the work of Sachdeva et al. (2019) and select two Carrington Rotations representative of a period of high solar magnetic activity for which to simulate the solar wind plasma background with AWSoM. We discuss the features of the model in the next section and describe the magnetic field maps used for the simulations in section 2.1. In sections 2.2 and 2.3 we describe the simulation setup and boundary condi-

tions for the model, respectively. We compare the results of the simulation with observations in the low corona, which includes extreme ultraviolet (EUV) images from SDO/AIA and demonstrate the temperature anisotropy due to energy partitioning within AWSoM. We also compare the solar wind parameters from the model with the observational data from OMNI database and STEREO-A/B spacecrafts. These results are presented in Section 3 followed by a summary in Section 4. The appendix describes our new approach of splitting the magnetic field in AWSoM.

2. ALFVÉN WAVE SOLAR ATMOSPHERE MODEL (AWSOM)

For our work, we apply numerical models developed at the University of Michigan, which are encompassed in the Space Weather Modeling Framework (SWMF; Tóth et al. 2005, 2012; Gombosi et al. 2021). SWMF is a software framework for physics-based space weather modeling and is composed of numerical models that cover a variety of physics domains that can be coupled with each other. In this paper, we use AWSoM to model the solar wind background in the Solar Corona (SC) and the Inner Heliosphere (IH) components within the SWMF.

AWSoM (van der Holst et al. 2014) is a self-consistent, 3D global extended MHD model with its inner boundary at the lower transition region extending into the solar corona and the heliosphere. AWSoM incorporates low-frequency reflection-driven Alfvén wave turbulence, proton temperature anisotropy (parallel and perpendicular proton temperatures), heat conduction and radiative cooling. The full set of MHD equations are solved using the numerical Block Adaptive Tree Solarwind-Roe-Upwind Scheme (BATS-R-US; Powell et al. 1999). The reader is referred to van der Holst et al. (2014) for a complete description of the equations and implementation. Over the years, AWSoM has transitioned from a two temperature (electrons and ions) model (van der Holst et al. 2010; Jin et al. 2012) to a three temperature model that accounts for the ion temperature anisotropy (Meng et al. 2015). The energy partitioning scheme in AWSoM has been significantly improved and validated against the data from the Parker Solar Probe (van der Holst et al. 2019, 2021). These improvements include using the critical balance formulation of Lithwick et al. 2007. In van der Holst et al. (2021), the wave period is set to the cascade time of the minor wave at the proton gyro radius scale instead of the major wave resulting in more electron heating and parallel proton heating and less perpendicular proton heating.

Over the years, AWSoM has been extensively validated for both solar minimum and solar maximum activ-
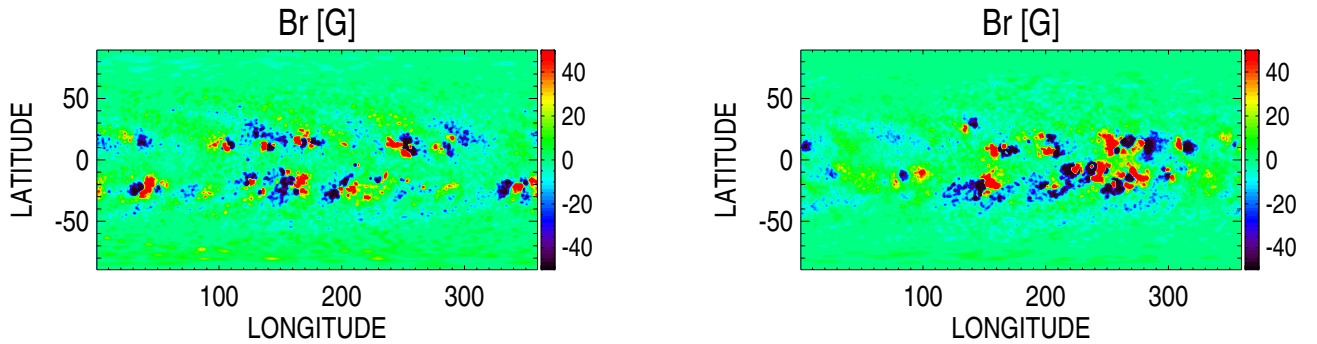
(a) Realization map 01 for CR2123 ADAPT-HMI map

(b) Realization map 12 for CR2152 ADAPT-HMI map

Figure 1. Radial magnetic field at R=1 R$_\odot$ for (a) CR2123 and (b) CR2152. Realization maps 1 and 12 of the ADAPT-HMI ensemble are chosen for the two rotations respectively. The radial magnetic field (Br) in this plot is saturated at $\pm$ 50 G.

ity periods (van der Holst et al. 2010; Meng et al. 2015; Jin et al. 2017; Sachdeva et al. 2019) by comparing the model simulated results with a variety of observations spanning the low corona and the inner heliosphere. Near the Sun, the simulated density and temperature of the solar corona are compared to reconstructions based on EUV observational data from STEREO-A/B, SDO/AIA and SOHO/LASCO (Sachdeva et al. 2019). Lloveras et al. 2017, 2020 compared the thermodynamic structure of the AWSoM simulated quiescent inner solar corona with the tomographic reconstructions of the electron density and temperature using Differential Emission Measure Tomography. In the inner heliosphere, AWSoM successfully reproduces the velocity observations of InterPlanetary Scintillation (IPS) data and the *in situ* solar wind plasma parameters observed at 1 AU (Jin et al. 2017; Sachdeva et al. 2019).

2.1. *Solar Magnetic Field Maps*

AWSoM is a data-driven model and requires the initial radial component of the magnetic field at the inner boundary. Like most solar corona models, this input comes from the solar synoptic/synchronic magnetic field maps, which are essential to drive these models and to make reliable predictions. Consequently, any uncertainties in the photospheric magnetic field measurements impacts the near-Sun as well as the space weather predictions (Bertello et al. 2014). Worden & Harvey (2000) developed evolving synoptic maps that improve the distribution of magnetic flux on the solar surface while the maps are continuously updated using observations. The ADAPT model (Arge et al. 2010, 2013; Henney et al. 2012) uses the Worden & Harvey (2000) model, which incorporates the effects of so-

lar differential rotation profile, supergranular diffusion, meridional flow, and random emergence of small-scale (background) flux elements to produce synchronic maps. They use the Los Alamos National Lab (LANL) data assimilation code (Arge et al. 2010) to provide multiple realizations, each corresponding to different model parameters and their associated uncertainties. The realizations evolve smoothly over time, independent of each other, without abrupt changes. The changes for any given realization (from one rotation to another) are driven smoothly by different supergranulation flow patterns. ADAPT maps using observations from different instruments are available at https://www.nso.edu/data/nisp-data/adapt-maps.

In this work, we simulate solar maximum conditions represented by Carrington rotations CR2123 and CR2152, corresponding to the time periods between 2012-04-28 to 2012-05-25 and 2014-06-28 to 2014-07-25, respectively. These rotations are periods when the Sun was populated by strong active regions and enhanced activity. For instance, an M-class flare on 2012-05-17 led to a halo CME eruption during CR2123 period (Gopalswamy et al. 2015). Another eruption on 2014-07-08 associated with an M-class flare was observed during CR2152. In Sachdeva et al. (2019), we show a comparison between the solar wind background produced by AWSoM using GONG and ADAPT-GONG magnetograms. The improved results with the ADAPT-GONG maps encourage us to use ADAPT products for our solar maximum runs. We include in this work for the first time, AWSoM results using ADAPT-HMI maps. Figure 1 shows the input radial magnetic field maps used for CR2123 and CR2152 using ADAPT-HMI maps. The best realization for each of the rotations are

chosen based on a quantitative comparison of AWSoM predicted solar wind parameters (using each realization as the initial condition) with OMNI data at 1 AU.

2.2. Boundary Conditions

The magnetic field map is used to set the boundary conditions, in particular the radial component of the magnetic field, at the inner boundary of the spherical grid of AWSoM. For sake of improved numerical accuracy, the magnetic field $\mathbf{B}$ is split into two variables: $\mathbf{B}_0$ is an analytic function that matches the boundary conditions, while $\mathbf{B}_1 = \mathbf{B} - \mathbf{B}_0$ is the difference between the numerical solution of the extended MHD equations and the analytic function. The traditional splitting (Tanaka 1994) requires that $\mathbf{B}_0$ is both divergence free and curl free, and it does not change in time. Some of these restrictions can be relaxed, and in fact in our previous work $\mathbf{B}_0$ was obtained as a Potential Field Source Surface (PFSS) solution with the source surface (where the potential field is forced to be radial) set to $R_{ss} = 2.5$ $R_\odot$ and the magnetic field is continued radially as $\mathbf{B}_0(r, \theta, \phi) = \mathbf{B}_0(R_{ss}, \theta, \phi)(R_{ss}/r)^2$ for $r > R_{ss}$. This approach results in non-zero curl of $\mathbf{B}_0$ at the source surface as well as along the current sheets formed outside the source surface. The non-zero $\mathbf{j}_0 = \nabla \times \mathbf{B}_0$ is taken into account in the momentum and energy equations (Gombosi et al. 2004).

While this approach is analytically correct, there are some undesirable numerical consequences. The non-zero $\mathbf{j}_0$ at the source surface has to be compensated by $\mathbf{j} = \nabla \times \mathbf{B}_1$, which may lead to inaccuracy in $\mathbf{B}_1$ and the total field $\mathbf{B}$. Switching from $\nabla \times \mathbf{B}_0 = 0$ to a non-zero $\nabla \times \mathbf{B}_0$ at the source surface requires a complex algorithm, because for some cells the effect of $\nabla \times \mathbf{B}_0$ should be removed, while for other cells it should be added. One can also discretize the effect of $\mathbf{B}_0 \times \nabla \times \mathbf{B}_0$ in alternative forms (divergence of a Maxwell tensor) and the optimal choice is not obvious.

Our new approach, first used in this work, is to move the source surface outside the domain of the solar corona (SC) model that typically has a radial extent of $24 R_\odot$, so we use $R_{ss} = 25$ $R_\odot$. This eliminates the non-zero curl of B_0 in the SC domain and minimizes the numerical artifacts. In other words, $\mathbf{B}_0$ captures the field near the solar surface and allows accurate representation of the strong fields near the active regions but it does not need to be representative of the heliospheric current sheet or the helmet streamer. Those features are best captured by the B_1 field obtained by solving the MHD equations.

The PFSS solution can be obtained using either spherical harmonics or the finite difference iterative potential field solver (FDIPS) (Tóth, van der Holst & Huang 2011). In this study, we use FDIPS to obtain the PFSS solution for the two rotations. The solution is calculated and stored on a spherical grid that extends from the solar surface at $r = 1$ $R_\odot$ to R_{ss}. AWSoM then interpolates this discrete solution to its own non-uniform adaptive grid. We use tri-linear interpolation of the $\mathbf{B}_{0x}$, $\mathbf{B}_{0y}$ and $\mathbf{B}_{0z}$ quantities stored on the spherical grid. Using the Cartesian components instead of spherical components avoids issues of interpolation near the poles. With the extended radial domain, using a uniform radial grid to calculate and store $\mathbf{B}_0$ is no longer optimal: the required resolution near the solar surface would lead to an excessively large radial grid resolution. To reduce the computational cost (both in storage and calculation time), we switched to a logarithmic radial coordinate, which provides the required accuracy with a similar grid size as we used previously for $R_{ss} = 2.5$ $R_\odot$. See the appendix for more detail.

At the inner boundary, the initial temperature for both isotropic electron and anisotropic (perpendicular and parallel) proton is set to 50,000 K. For the solar corona model, this selected temperature value in the lower transition region is low enough to generate EUV images without any distortions. This is important for validation efforts of simulated results near the Sun. The selected temperature value is also high enough to not be affected by the complex physical processes in the chromosphere. The proton number density is overestimated and set to 5×10^{18} m^{-3}. This overestimation does not effect the coronal solution (Lionello et al. 2009) and is required to avoid chromospheric evaporation (Sokolov et al. 2013; van der Holst et al. 2014). To avoid a strong density jump at the inner boundary, AWSoM is initialized with an exponentially stratified atmosphere connected to the Parker solution. The temperature profile remains flat while the density falls off exponentially till the effects of radiative cooling is not significant enough so as to cool the temperature below 50,000 K. As AWSoM relaxes from the initial conditions to the final steady state, the physically meaningful inner boundary moves upwards to where the temperature begins to rise above 50,000 K.

The energy density of the outgoing Alfvén wave is set through the Poynting flux (S_A) of the outward propagating wave at the inner boundary. AWSoM sets S_A to be proportional to $B_\odot$, the magnetic field strength at the inner boundary (Fisk 1996, 2001; Fisk and Schwadron 2001; Fisk, Schwadron & Zurbuchen 1999a; Fisk, Zurbuchen & Schwadron 1999b; Sokolov et al. 2013). The proportionality factor $(S_A/B)_\odot$ is an adjustable parameter of AWSoM. From our simulations we find that the stronger magnetic field of the Sun during periods of

higher activity requires $(S_A/B)_\odot$ to be lowered compared to $10^6 W m^{-2} T^{-1}$ used for solar minimum simulations (Sachdeva et al. 2019). The parameter $(S_A/B)_\odot$ in the solar maximum simulations is set to 0.5 and $0.4 \times 10^6 W m^{-2} T^{-1}$ for CR2123 and CR2152, respectively. Higher Poynting flux leads to a deposition of excess energy density into the chromosphere, which may lead to unphysically high density peaks at 1 AU. We discuss these results later in the paper. The Alfvén wave correlation length ($L_\perp$) which is transverse to the magnetic field direction is proportional to $B^{-1/2}$ (Hollweg 1986). This proportionality constant ($L_\perp \sqrt{B}$) is an adjustable input parameter in the model which is set to 1.5×10^5 m $\sqrt{T}$. To account for the energy partitioning between electrons and protons, the stochastic heating exponent and amplitude (Chandran et al. 2011) are set to 0.21 and 0.18 respectively.

2.3. *Details of the SC-IH Coupling*

We use AWSoM to run the SC and IH components of SWMF. The SC to IH coupling employs a spherical buffer grid between 18 and 21 R$_\odot$. The SC component uses a 3D spherical grid extending from 1 - 24 R$_\odot$ and the IH component uses a Cartesian grid that extends from -250 to 250 R$_\odot$ with an inner boundary at 20 R$_\odot$ covered by the buffer grid. The SC domain is decomposed into grid blocks consisting of 6×8×8 grid cells, while IH has 8×8×8 sized blocks. The grid uses Adaptive Mesh Refinement (AMR). The angular resolution is 1.4° below 1.7 R$_\odot$ and 2.8° in the remaining domain of SC. The cell size in IH ranges between 0.48 R$_\odot$ near the inner boundary and 7.8 R$_\odot$ at the outer boundaries. In addition to the geometric AMR, the current sheet is adaptively resolved with 1.4° resolution in SC and 1 R$_\odot$ resolution in IH. The total number of grid cells in SC and IH are about 4.7 million and 28 million, respectively.

Both SC and IH solve the extended MHD equations in co-rotating frames, where a steady state solution can be obtained. The contributions from the Coriolis and centrifugal forces are included into the equations as source terms. Using local time stepping, the SC component is run for 80,000 iterations to get a steady state. Next, SC is coupled with IH for one step followed by 5,000 iterations in IH to obtain a steady state solution in IH as well. We note that the solar wind is super fast magnetosonic in the IH domain, so the solution converges very fast, unlike SC.

To improve the accuracy of the solution near the Sun, we increase the angular resolution of the grid below 1.7 R$_\odot$ to 0.7° and switch to the fifth-order-accurate numerical scheme (Chen, Tóth & Gombosi 2016) within 1.7 R$_\odot$. The standard second-order shock-capturing scheme (Linde with Koren's limiter) is used in the remainder of the SC region (Tóth et al. 2012). Another 20,000 iterations are performed to relax the solution to the final improved steady state. The improvement is most significant in the synthetic line of sight (LOS) EUV images produced by the model. The following section describes the results of the steady-state simulations for the solar maximum conditions using AWSoM.

3. RESULTS

We simulate the background solar wind in the solar corona and the inner heliosphere for Carrington Rotations CR2123 and CR2152 using AWSoM and compare the results to data from various observational sources. These rotations are representative of periods of high magnetic activity of the Sun. The physical process of wave dissipation, heat conduction and radiative cooling within AWSoM facilitates simulating the temperature and density structure of the solar corona. AWSoM can produce synthetic EUV images that can be compared with the EUV observations from SDO/AIA and STEREO-EUVI. In the steady-state configuration, the AWSoM model results can be extracted along the trajectories of any given planet/satellite. We compare the simulation output along the STEREO A and B orbits and also with the solar wind plasma observations from the OMNI database.

Figure 2 shows the AWSoM model simulation output comparison with EUV observations from the SDO/AIA spacecraft. We show the results in six different wavelength channels. Our model reproduces the overall brightness and location of the various active regions quite well. AWSoM does not include any stray-light correction function and the model assumes that for all wavelengths the plasma is optically thin. We see that the coronal holes in the simulation are darker compared to the observations, which may in part be due to neglecting the stray-light component caused by long-range scatter in the observations.

Figure 3 shows the comparison of synthetic EUV images obtained from the AWSoM simulation with the STEREO-A/B EUVI observations in three wavelength channels (171, 195 and 284 A°) for both the rotations. The observations have been corrected for stray-light due to long-range scattering. In the case of the EUVI detectors, stray-light has been shown to significantly contribute to the signal in coronal holes seen on the solar disk and its correction is part of the processing pipeline (Shearer et al. 2012). For CR2123, the STEREO-A and B spacecrafts were separated from Earth by ≈ 117° and 114° respectively. For CR2152, both the STEREO-A and B spacecrafts were separated from Earth by an an-
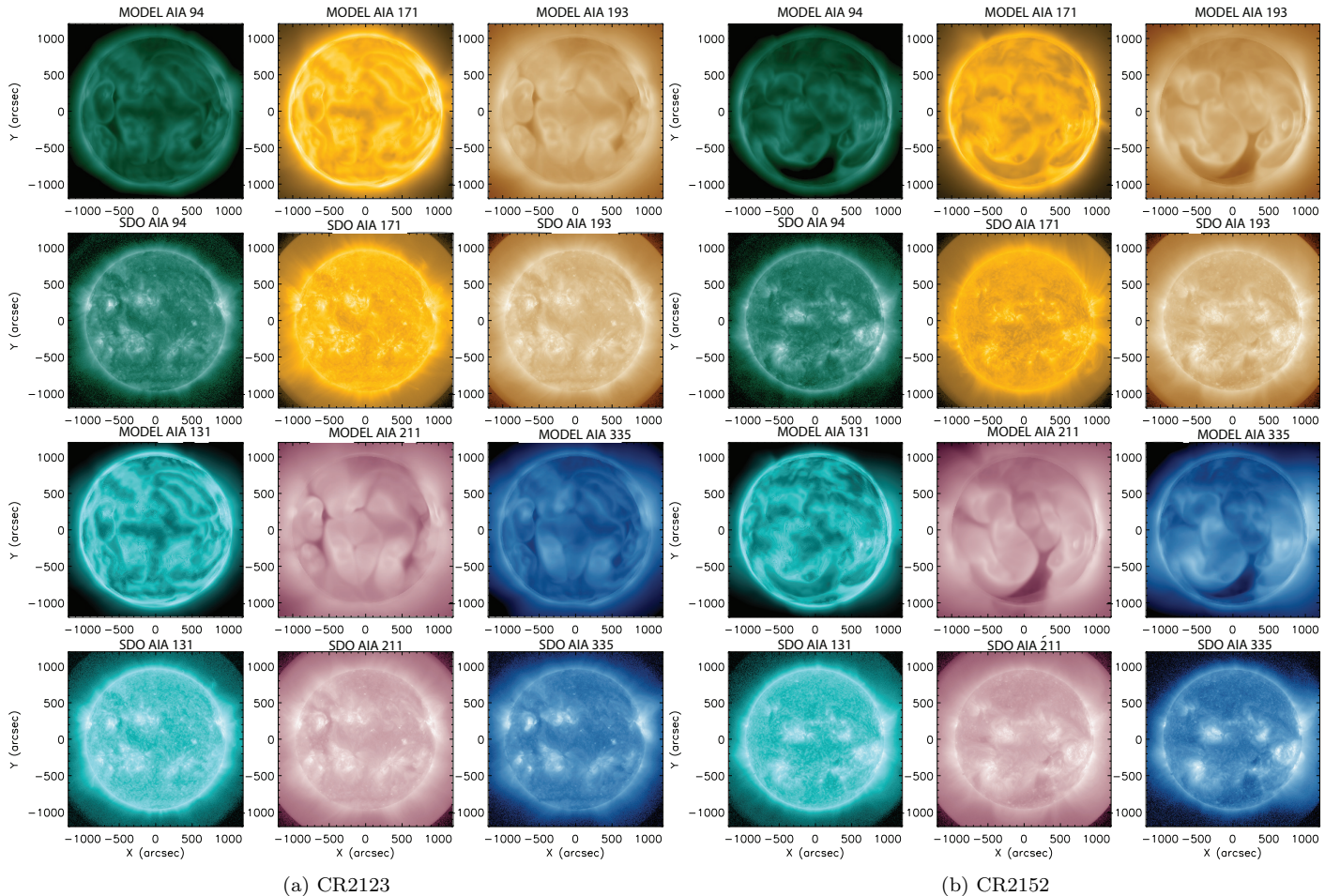
Figure 2. Comparison between AWSoM simulated LOS EUV results and SDO/AIA observations for (a) CR2123 and (b) CR2152. The ADAPT-HMI map realizations used for CR2123 and CR2152 are 01 and 12 respectively. Figures (a) and (b) compares AWSoM LOS (rows 1 and 3) with the SDO/AIA observations (rows 2 and 4) in multiple wavelengths (94,171,193,131,211,335 Å).

gle of ≈ 162° and located behind the Sun. We see that the location of the coronal holes and the major active regions is reproduced in the model for CR2123. For CR2152, the model does not show the major bright active regions. The overall brightness is comparable with the observations for both the rotations, however, we find that not all active regions are as bright in the synthetic EUV images as observed during solar maximum and the major coronal holes are darker in the synthetic images.

As described in Section 2, the energy partitioning distributes the heating from the turbulent dissipation in AWSoM over three temperatures. These are the perpendicular and parallel (to the magnetic field) ion temperatures ($T_\perp$ and $T_{||}$) and the electron temperature (T_e). Figure 4 shows these temperatures on a meridional slice (X=0 plane) for CR2152. We limit the distance range between -10 $R_\odot$ to 10 $R_\odot$ in these figures to emphasise

the features. Due to highly frequent Coulomb collisions near the Sun, the three temperatures tend to equilibrate, as confirmed by the plots. Further out, the collisions become more infrequent which no longer supports the equilibrium and the temperatures diverge. The parallel component of ion temperature $T_{||}$ is significant in regions close to the heliospheric current sheet where the plasma beta is high. As we move away from the Sun, stochastic heating leads to an increase in the ion perpendicular temperature $T_\perp$. Protons are heated more in the direction perpendicular to the magnetic field in regions away from the Sun and the heliospheric current sheet. The electrons are significantly heated very close to the Sun and around the heliospheric current sheet. Figure 5 shows the ratio of the perpendicular and parallel components of the ion temperature. Near the Sun, the ratio is close to 1 and increases as we move away from the Sun and the heliospheric current sheet.

(a) CR2123 STA-EUVI

(b) CR2123 STB-EUVI

(c) CR2152 STA-EUVI

(d) CR2152 STB-EUVI
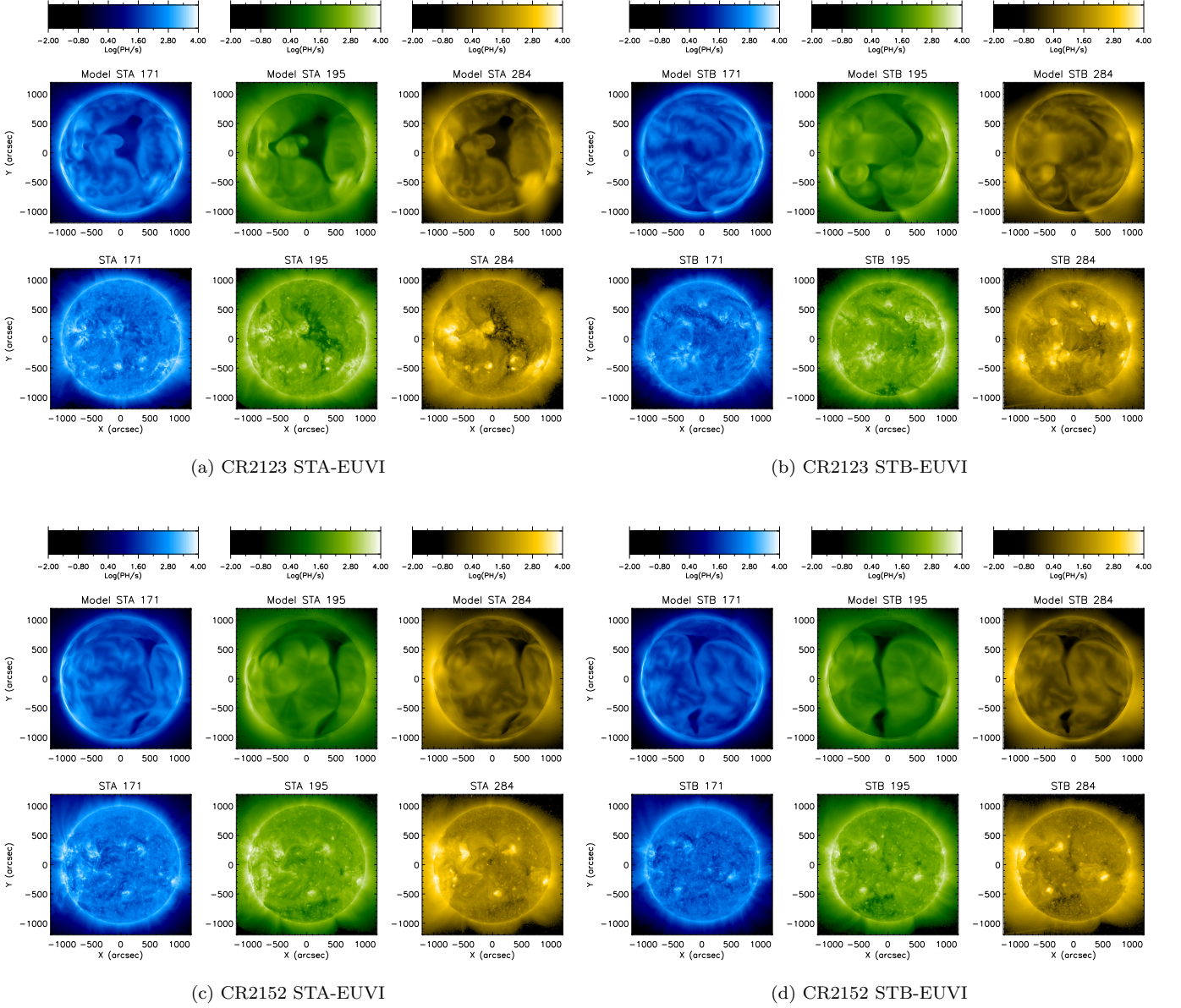
Figure 3. Data-Model comparisons for CR2123 and CR2152 with STEREO-A and B EUVI observations. Figures (a) and (b) show the comparison between the synthetic EUV images obtained from AWSoM simulation (top row) and the stray-light corrected observations (bottom row) from STEREO-A and B respectively in three wavelength channels for CR2123. Figures (c) and (d) show the same comparison for CR2152.

Figures 6 and 7 present the comparisons between AWSoM simulation results and the observations of solar wind plasma parameters for CR2123 and CR2152. Figure 6 shows the AWSoM results (in red) at the location of the Earth and the solar wind observations from the OMNI database (in black). AWSoM reproduces the steady-state solar wind quite well for both these rotations that represent periods of higher magnetic activity. Overall the model compares reasonably with the observations in predicting the solar wind speed (Ur), proton density (Np) and temperature at 1 AU. AW-

SoM underestimates the total magnetic field (B) for both rotations. In the left panel of Figure 6 the observations for CR2123 show a high speed stream around 2012-05-22 that is completely missed by AWSoM. In the right panel of Figure 6 for CR2152, the simulated output along 1 AU shows elevated speeds corresponding to low density profile while the observations do not show any such features. Our coronal model is driven by observations of the photospheric magnetic field and not constrained by plasma observations at 1 AU. Therefore, not all observed features are always reproduced by the
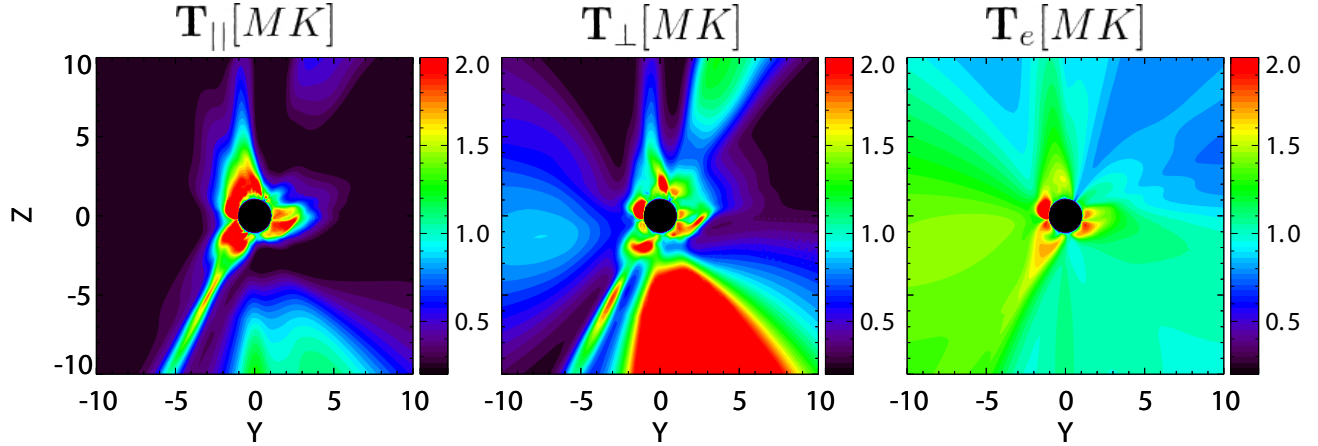
Figure 4. The figure shows the meridional slice (X=0 plane) between -10 $R_\odot$ to 10 $R_\odot$ depicting the three temperatures in the low corona. The three panels are ion temperature parallel to the B field ($T_{||}$), perpendicular ion temperature ($T_\perp$) and the isotropic electron temperature (T_e). All variables are in units of 10^6 K. These results are shown for CR2152.
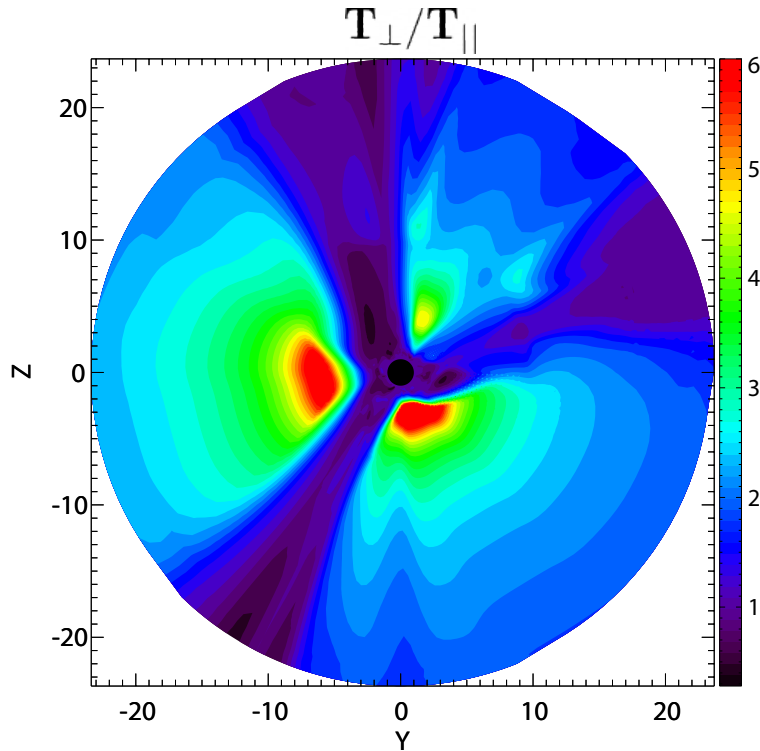
Figure 5. Meridional slice (X=0 plane) in the SC component depicting the ratio of the perpendicular ($T_\perp$) and parallel ($T_{||}$) components of ion temperature for CR2152.

model. Figure 7 shows the same set of plasma parameters observed from STEREO-A and B. Observational data is shown in black while AWSoM results are shown in red for the two rotations. We find a good comparison between STEREO observations and the AWSoM model results. For both rotations, the model underestimates the proton temperature observed in STEREO-A and B. The straight black line (between 06-Jul-2014 and 11-Jul-2014) in Figure 7 panel (b) is due to partially missing data. In each panel of Figures 6 and 7, we indicate a quantity Dist to characterize the error between observations and the model output. Dist is the distance between two curves in a plane independent of the coordinate system so that the temporal and spatial coordinates are treated equally (see Sachdeva et al. (2019) for more detail). We use this quantitative measure to determine the
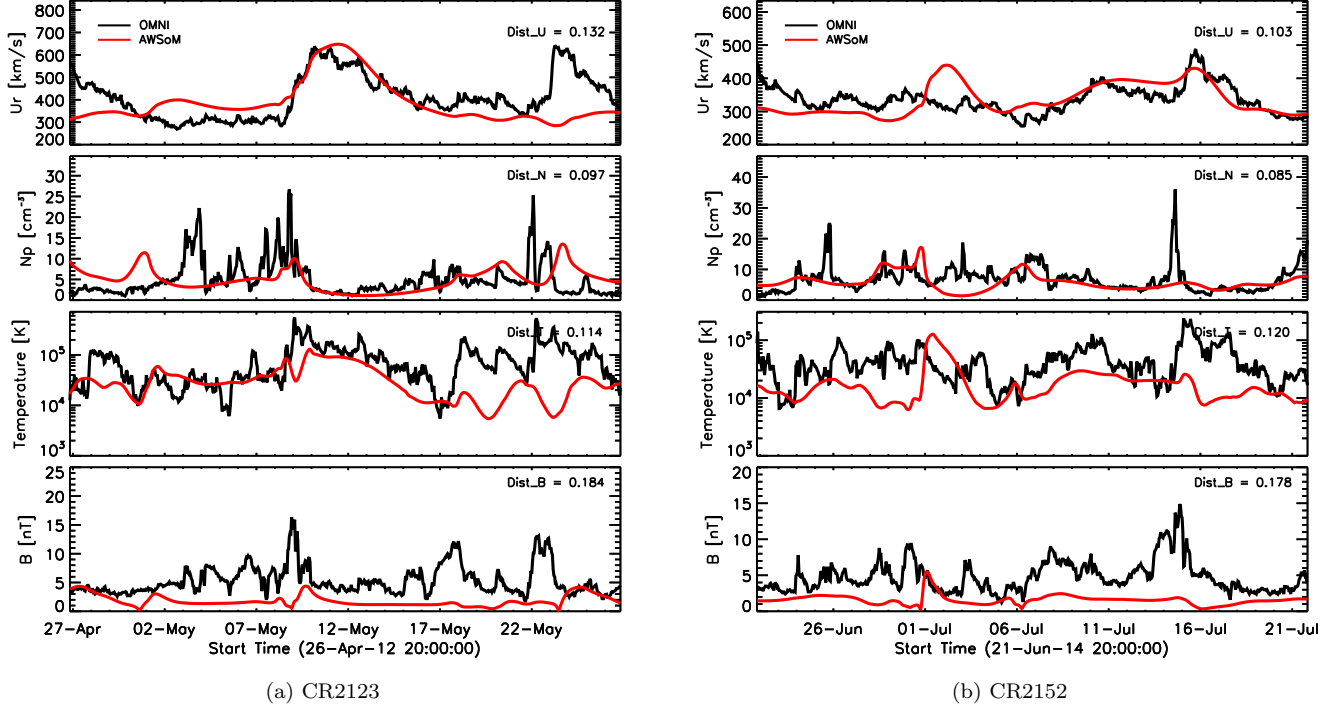
Figure 6. Data-Model comparisons for CR2123 and CR2152 at 1 AU. Figures (a) and (b) show the AWSoM results (in red) along the trajectory of the Earth and the solar wind plasma observations from the OMNI database (in black).

best ADAPT realization out of the 12 available maps for each rotation. The results shown here use the ADAPT map realizations with the smallest distance in solar wind speed (Dist_U) and proton density parameters (Dist_N) between the model and observations.

In our simulations of different phases of the solar cycle, we find that to obtain good comparisons with observations, the Poynting flux $(S_A/B)_\odot$ parameter needs to be modified compared to the optimal values that were used for the solar minimum rotations in Sachdeva et al. (2019). For solar minimum, the quantity $(S_A/B)_\odot$ was set to 1×10^6 Wm^{-2}T^{-1} which provided the best comparisons with various observations. When this value was used for the rotations studied in this paper, the simulations showed unphysical densities at 1 AU. The blue line in panel (a) of Figure 8 shows the 1 AU result for CR2152 using AWSoM model with $(S_A/B)_\odot = 1$ MWm^{-2}T^{-1}. We see very high density peaks and corresponding low speeds in those simulation results. The red line in the figure shows AWSoM results with $(S_A/B)_\odot$ decreased to 0.4 MWm^{-2}T^{-1} (same as panel (b) in Figure 6). We conclude that $(S_A/B)_\odot$ needs to be adjusted to reproduce the observed plasma parameters for solar maximum runs with AWSoM. This may also suggest that as the solar cycle tends toward the maximum phase the average magnetic field strength is higher in the solar wind source regions which requires

the amount of Poynting flux per B to be lowered. Huang et al. (2021) studies how the Poynting flux parameter $(S_A/B)_\odot$ changes during the last solar cycle and find that the optimal Poynting flux value for different rotations can be correlated with various characteristics of the solar magnetic field, such as open flux and area of coronal holes.

The major observational driver of solar corona models, including AWSoM, is the photospheric magnetic field map. There are multiple instruments providing photospheric field measurements and ensembles of magnetograms. However, there are various factors contributing to the uncertainties in these observations including limited observations of the polar regions of the Sun which requires empirical estimates to fill in the poles. The ADAPT model improves on these magnetic field maps by using data assimilation and including physical processes to compensate for the lack or limitations of observations. We use the ADAPT-GONG and ADAPT-HMI magnetograms for CR2152 to show how the results vary depending on which data product is used with the ADAPT model. Figure 8 shows the AWSoM simulation output at 1 AU using ADAPT-GONG (in red) and ADAPT-HMI (in blue) maps. The two simulations have the same model parameters except that the initial (and inner boundary) condition for the radial component of the magnetic field is supplied by ADAPT maps
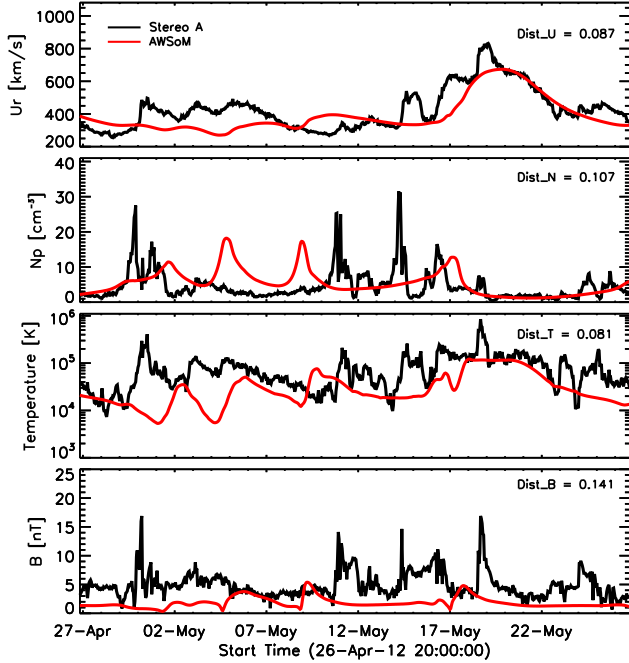
(a) CR2123
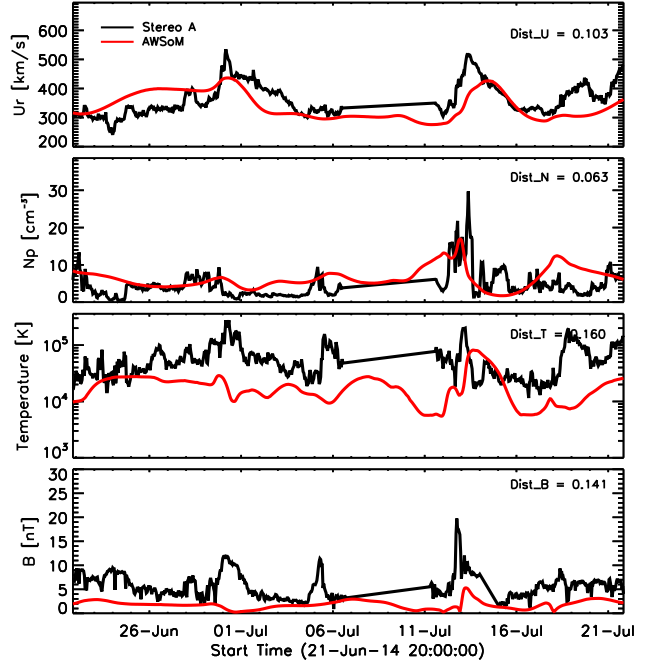
(b) CR2152
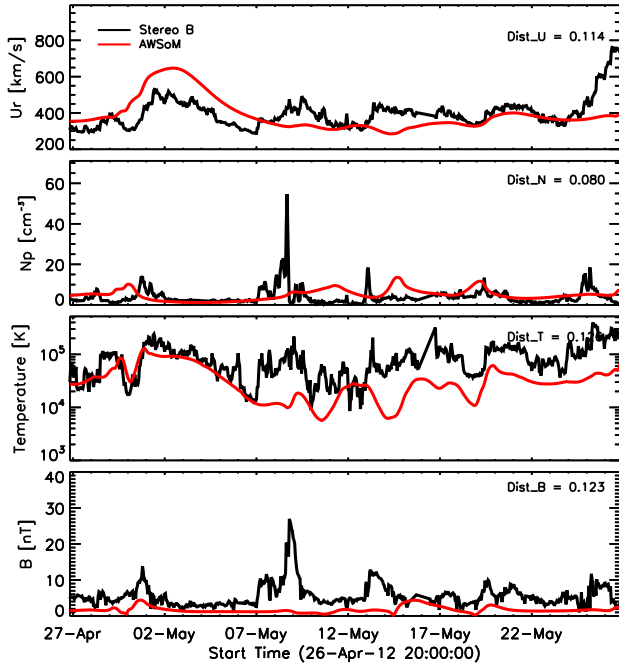
(c) CR2123
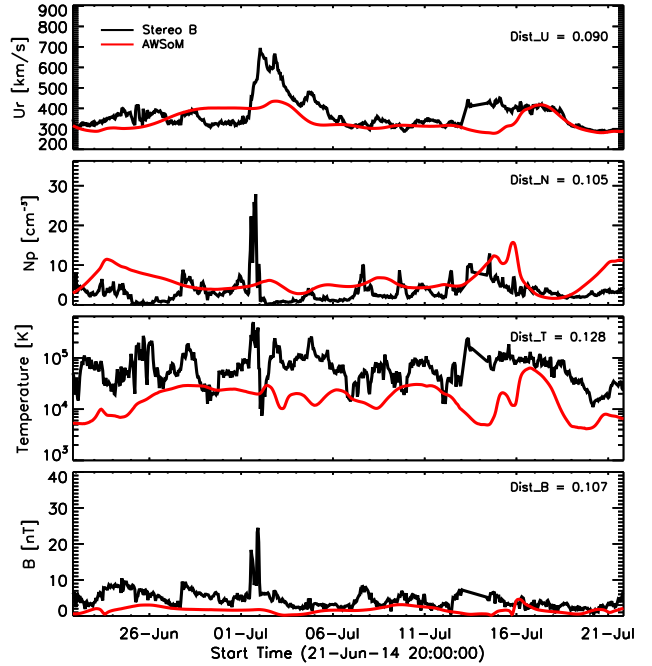
(d) CR2152

Figure 7. Data-Model comparisons for CR2123 and CR2152 with STEREO-A and B observations. Figures (a) and (b) show the AWSoM results (in red) along the trajectory of STEREO-A and the solar wind plasma observations from STEREO-A (in black) for CR2123 and CR2152 respectively. Figures (c) and (d) show the comparisons between AWSoM and STEREO-B data for the two rotations.

produced from two different instruments (GONG and HMI). The results demonstrate how the simulation so-

lution varies between the two cases using different magnetograms, as is especially displayed by the major dif-
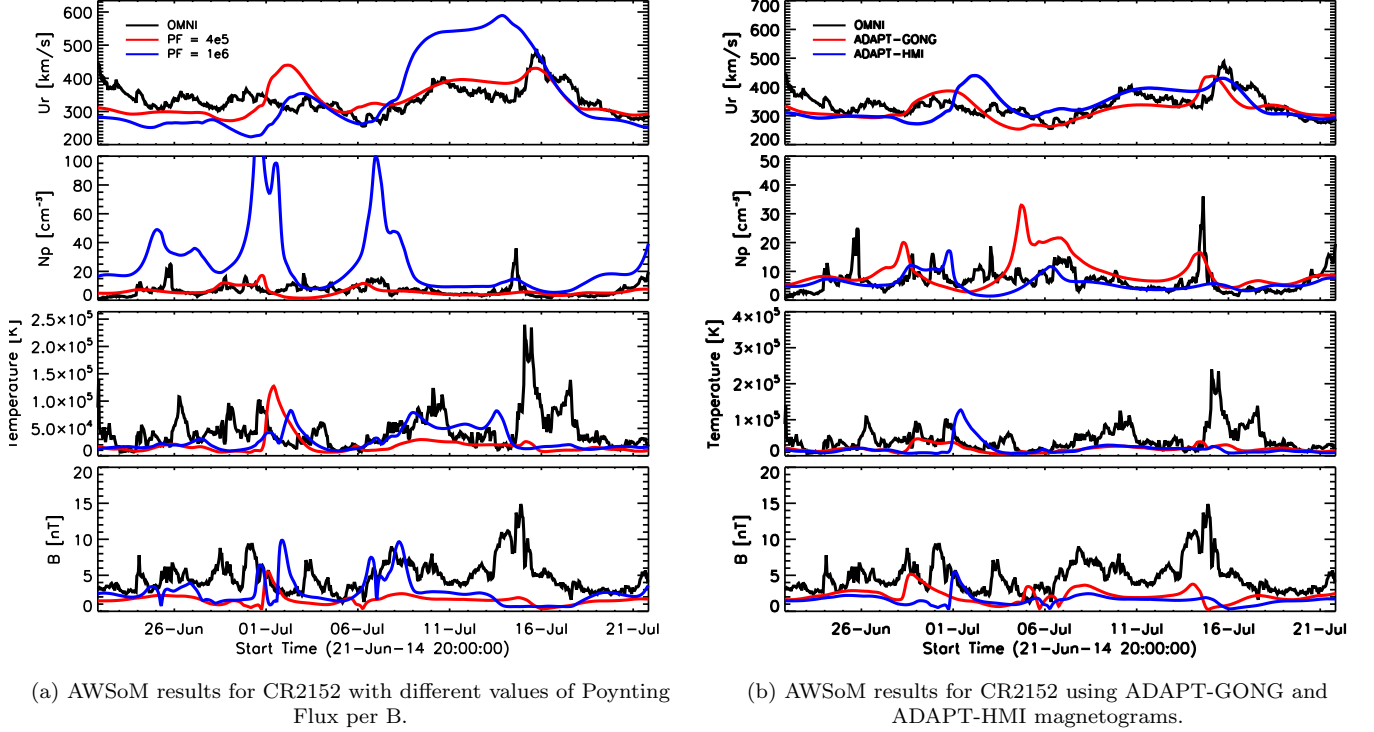
(a) AWSoM results for CR2152 with different values of Poynting Flux per B.

(b) AWSoM results for CR2152 using ADAPT-GONG and ADAPT-HMI magnetograms.

Figure 8. Data-Model comparisons for CR2152. Panel (a) shows the AWSoM simulation results at 1 AU using different values of the Poynting flux parameter $(S_A/B)_\odot$. The red line corresponds to $(S_A/B)_\odot = 4 \times 10^5$ Wm^{-2}T^{-1} (same as panel (b) in Figure 6) and the blue line corresponds to $(S_A/B)_\odot = 1 \times 10^6$ Wm^{-2}T^{-1} which is the optimal value used for solar minimum rotations. Panel (b) shows the AWSoM simulation results using ADAPT-GONG magnetogram (red line) and ADAPT-HMI magnetogram (blue line) using the same AWSoM parameters. OMNI data is shown in black.

ference in the proton density at 1 AU. The AWSoM output using ADAPT-GONG map (red) shows a speed profile comparable to the observations while the AW-SoM result with ADAPT-HMI (blue) slightly overestimates the speed. However, the lower speed (using ADAPT-GONG) is accompanied by very high density values compared to both ADAPT-HMI output and observations which severely impacts the background into which a CME may be launched. The temperature comparison is better in the case of ADAPT-HMI driven output with AWSoM and the magnetic field prediction is comparable for both cases.

4. SUMMARY AND DISCUSSION

In order to model CMEs and to accurately predict their arrival and impact at the Earth, it is crucial to first obtain the correct background solar wind solution into which the CMEs can propagate and evolve. Stronger CME events often occur during the phase of the solar cycle when the magnetic activity is high, so it is important to get good background solutions under these conditions. In this work, we chose two Carrington Rotations (CR2123 and CR2152) representative of this active time period and perform simulations of the solar corona and the inner heliosphere using the 3D extended MHD model AWSoM. We compare the AWSoM predicted solar wind to observations of solar corona structure near the Sun and solar wind plasma parameters near the Earth and at STEREO-A and B.

We use the ADAPT-HMI phototspheric magnetic field maps as observational input to the model for both the rotations. AWSoM simulation results provide the solar coronal temperature and density structure which is used to produce LOS images comparable to EUV observations. Comparing these synthetic LOS images obtained from AWSoM with the EUV observations from SDO/AIA, we find that our model reproduces the overall brightness, location and structure of the active regions. Further away from the Sun, we compare the AWSoM predicted solar wind parameters at 1 AU with the *in situ* spacecraft observations at L1 and by the STEREO-A and B spacecrafts. AWSoM underestimates the background magnetic field, however, we get a good match with the speed, proton density and temperature of the solar wind plasma. Therefore, AWSoM successfully predicts the solar wind background which is a crucial step towards establishing a plasma environment into which a CME can be propagated and evolved. We also show how

different values of the Poynting Flux parameter affect the solar wind comparison at 1 AU for solar maximum conditions. For the studied solar maximum, the optimal value of $(S_A/B)_\odot$ is about a factor of 2 smaller than the optimal value used for solar minimum conditions. Since most solar corona models are sensitive to the magnetic field observations that are used to drive them, we show how the 1 AU simulation results compare with observations and with each other when ADAPT-GONG and ADAPT-HMI maps are used.

This validation work is in preparation of simulating CMEs launched from the surface of the Sun into the background solar wind and study their evolution and space weather impacts. The good comparisons of AW-SoM simulated solar wind with observations at various radial distances between the Sun and the Earth suggest that our model is capable of reproducing observed solar wind plasma and can be used for space weather modeling and prediction purposes for both solar minimum and solar maximum phases of the solar cycle.

5. APPENDIX

In the simulation setup for the PFSS solution, we move the source surface out to 25 $R_\odot$ to prevent non-zero curl of B_0 inside the SC domain and avoid numerical artifacts (Section 2.2). The spherical grid used by the Finite Difference Iterative Potential field Solver (FDIPS, Tóth, van der Holst & Huang (2011)) extends from the inner boundary at 1 $R_\odot$ to the source surface where B_0 becomes radial. When the source surface radius is large, it is numerically beneficial to use a logarithmic radial grid spacing, since the solution varies fastest near the solar surface and it becomes smoother further out. Figure 9 shows the 1 AU simulation output for CR2123 using AWSoM model for four different cases. For each case, the source surface is set at 25 $R_\odot$, and the FDIPS grid for the PFSS solution is either logarithmic or linear in the radial direction with the number of points in the radial direction (nR) equal to either 180 or 400. The longitudinal and latitudinal resolution is same in all four cases.

In the figure, the red line corresponds to a logarithmic scale with nR=180 in the radial direction (case (a)), the blue line corresponds to logarithmic grid with nR=400 (case (b)) (same as panel (a) of Figure 6). The red line is made thicker for better visibility in the plot, because it mostly coincides with the blue line. Next, the pink line corresponds to a linear scale in the radial direction with nR=180 (case (c)) and finally, the cyan line corresponds to linear grid with nR=400 (case(d)). We find that doubling the number of grid points in the radial direction (cases (a) and (b)) does not provide any major advantage as long as the radial grid is logarithmic, so computer memory can be saved by using 180 grid points instead of 400. On the other hand, using a linear radial grid leads to significantly different and inaccurate results (cases (c) and (d)), even for 400 grid points. Although, the features in the output are at the same location as for the logarithmic grid, the magnitudes are much lower primarily due to the resolution being not fine enough near the solar surface. We also see an unphysical jump in the density corresponding to very low speeds in cases (c) and (d).

The same source surface radius and the same logarithmic radial grid can also be used to calculate $\mathbf{B}_0$ from spherical harmonics and then interpolate to the adaptive grid of AWSoM.

REFERENCES

Alazraki, G., & Couturier, P. 1971, A&A, 13, 380

Arge, C.N., Henney, C.J., Koller, J., et al. 2010, Twelfth International Solar Wind Conference 1216, AIP, Saint-Malo, France, 343

Arge, C.N., Henney, C.J., González Hernández, I., et al. 2013, Proceedings of the Thirteenth International Solar Wind Conference 1539, AIP, Big Island, Hawaii, 11

Belcher, J.W., & Davis, L., Jr. 1971, J. Geophys. Res., 76, 3534
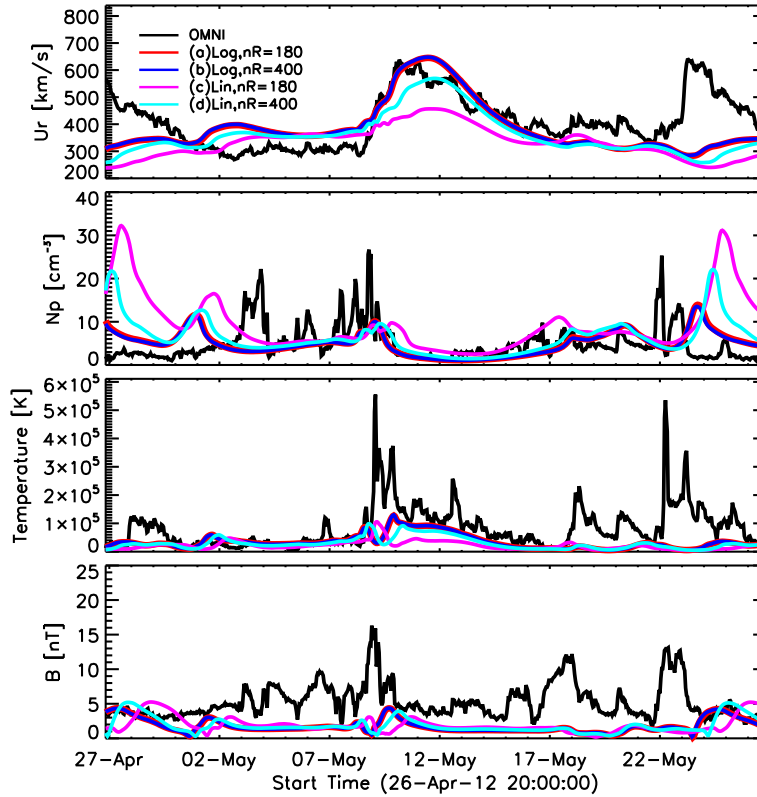
Figure 9. 1 AU simulation results using AWSoM for CR2123 for different cases of radial grid and resolution in the PFSS solution. The source surface for the PFSS model is set to 25 $R_\odot$ and the grid is same in the latitudinal and longitudinal directions for all the results. The red line corresponds to case (a) with logarithmic scale and nR=180 on the FDIPS grid setup. The line is made thicker for better visibility. Case (b) with logarithmic scale and nR=400 is represented by the blue line. Cases (c) and (d) correspond to a linear scale and nR=180 and nR=400 in the radial direction respectively. OMNI data is shown in black.

Bertello, L., Pevtsov, A. A., Petrie, G. J. D., et al. 2014, Sol. Phys., 289, 7

Bravo, S., & Stewart, G. A. 1997, ApJ, 489, 992

Brueckner, G. E., Howard, R. A., Koomen, M. J., et al. 1995, Sol. Phys., 162, 357

Chandran, B. D. G., Dennis, T. J., Quataert, E., & Bale, S. D. 2011, ApJ, 743, 197

Chen, Y., Tóth, G., Gombosi, T. I. 2016, J. Computational Phys., 305, 604

Cohen, O., Sokolov, I. V., Roussev, I. I., et al. 2007, ApJL, 654, L163

Coleman, P.J. 1968, ApJ, 153, 371

Cranmer, S.R 2010, ApJ, 710, 676

Downs, C., Roussev, I.I., van der Holst, B., et al. 2010, ApJ, 712, 1219

Evans, R.M., Opher, M., Oran, R., et al. 2012, ApJ, 756, 155

Feng, X., Zhang, S., Xiang, C., et al. 2011, ApJ, 734, 50

Fisk, L. A. 1996, JGR, 101, 15, 547

Fisk, L. A. 2001, JGR, 106, 15, 849

Fisk, L. A., Schwadron, N. A. 2001, ApJ, 560, 425

Fisk, L. A., Schwadron, N. A., and Zurbuchen, T. H. 1999a, JGR, 104, 19, 765

Fisk, L. A., Zurbuchen, T. H., and Schwadron, N. A. 1999b, ApJ, 521, 868

Gombosi, T. I., Powell, K. G., De Zeeuw, D. L., et al. 2004, Computing in Science Engineering, 6, 14

Gombosi T. I., van der Holst B., Manchester W. B. & Sokolov I. V. 2018, LRSP, 15, 4

Gombosi T. I., Chen, Y., Glocer, A., et al. 2021, JSWSC, accepted for publication

Gopalswamy, N., Makela, P., Akiyama, S., et al. 2015, Sun and Geospace, 10, 111

Groth, C. P. T., DeZeeuw, D. L., Gombosi, T. I., et al. 2000, J. Geophys. Res., 105, 25053

Henney, C. J., Toussaint, W. A., White, S. M., et al. 2012, Space Weather: The International Journal of Research and Applications, 10, S02011

Hollweg, J. V. 1986, JGR Space Physics, 91, 4111

Howard, R. A., Moses, J. D., Vourlidas, A., et al. 2008, SSRv, 136, 67

Huang, Z. 2021, ApJ, *in preparation*

Jian, L. K., MacNeice, P. J., Mays, M. L., et al. 2016, Space Weather, 14, 592

Jin, M., Manchester IV, W.B., van der Holst, B., et al. 2012, ApJ, 745,6

Jin, M., Manchester IV, W. B., van der Holst, B., et al. , ApJ, 2017, 834, 172

Kilpua E., Koskinen H. E. J. & Pulkkinen T. I. 2017, LRSP, 14, 5

Leer, E., & Axford, W.I. 1972, Sol. Phys., 23, 238

Lemen, J. R., Title, A. M., Akin, D. J., et al. 2012, SoPh, 275, 17

Li, B., Li, X., Hu, Y.-Q., & Habbal, S.R. 2004, J. Geophys. Res., 109, A07103

Lionello, R., Linker, J.A., & Mikíc, Z. 2009, ApJ, 690, 902

Lithwick, Y., Goldreich, P., & Sridhar, S. 2007, ApJ, 655, 269

Lloveras, D. G., Vásquez, A. M., Nuevo, F. A., et al. 2017, Sol. Phys., 292, 153

Lloveras, D. G., Vásquez, A. M., Nuevo, F. A., et al. 2020, Sol. Phys., 295, 76

Manchester IV, W. B., Kilpua, E. K. J., Liu, Y. D., et al. 2017, Space Sci Rev, 212, 1159

Matsumoto, T., & Suzuki, T.K. 2012, ApJ, 749, 8

Matthaeus, W. H., Zank, G. P., Oughton, S., et al. 1999, ApJL, 523, L93

Meng, X., van der Holst, B., Tóth, G.,& Gombosi, T. I. 2015, MNRAS, 454, 3697

Mikić, Z., Linker, J. A., Schnacl, D. D., et al. 1999, Physics of Plasmas, 6, 2217

Oran, R., van der Holst, B., Landi, E., et al. 2013, ApJ, 778, 176

Powell, K. G., Roe, P. L., Linde, T. J., et al. 1999, JCoPh, 154, 284

Roussev, I. I., Gombosi, T. I., Sokolov, I. V., et al. 2003, ApJL, 595, L57

Ruderman, M. S., Nakariakov, V. M., & Roberts, B. 1998, A&A, 338, 1118

Sachdeva, N., van der Holst, B., Manchester, W. B., et al. 2019, ApJ, 887, 83

Schou,J., Scherrer, P. H., Bush, R. I., et al. 2012, Sol. Phys., 275, 229

Shearer, P., Frazin, R. A., Hero III, A. O., et . al. 2012, ApJ, 749, 8

Sokolov, I.V., van der Holst, B., Oran, R., et al. 2013, ApJ, 764, 23

Suzuki, T.K., & Inutsuka, S.-i. 2006, J. Geophys. Res., 111, A06101

Tanaka, T. 1994, JCP, 111, 381

Tóth, G., Sokolov, I. V., Gombosi, T. I., et al. 2005, J. Geophys. Res., 110, A12226

Tóth, G., van der Holst, B., Huang, Z., 2011, ApJ, 732, 102

Tóth, G., van der Holst, B., Sokolov, I.V., et al. 2012, J. Comp. Phys., 231, 870

Usmanov, A.V., Goldstein, M.L., Besser, B.P., & Fritzer, J.M. 2000, J. Geophys. Res., 105, 12675

van der Holst, B., Manchester IV, W.B., Frazin, R.A., et al. 2010, ApJ, 725, 1373

van der Holst, B., Sokolov, I. V., Meng, X., et al. 2014, ApJ, 782, 81

van der Holst, B., Manchester, W. B., IV, Klein, K. G., et al., 2019, ApJL, 872, L18

van der Holst et al., B., Huang, J., Sachdeva, N., et al., 2021, submitted to ApJ, under review.

Vásquez, A.M., van Ballegooijen, A.A., & Raymond, J.C. 2003, ApJ, 598, 1361

Velli, M., Grappin, R., & Mangeney, A. 1989 Phys. Rev. Lett., 63, 1807

Verdini, A., & Velli, M. 2007, ApJ, 662, 669

Worden, J. & Harvey, J. 2000, Sol. Phys., 195, 2

Zank, G. P., Matthaeus, W.H., Smith, C. W. 1996, J. Geophys. Res., 101, 17093